

# Scaling relations and spectral characteristics of tensile microseisms: evidence for opening/closing cracks during hydraulic fracturing

David W. Eaton,<sup>1</sup> Mirko van der Baan,<sup>2</sup> Brad Birkelo<sup>3</sup> and Jean-Baptiste Tary<sup>2</sup>

<sup>1</sup>*Department of Geoscience, University of Calgary, Calgary, Alberta, Canada T2N 1N4. E-mail: eatond@ucalgary.ca*

<sup>2</sup>*Department of Physics, University of Alberta, Edmonton, Alberta, Canada T6G 2R3*

<sup>3</sup>*Spectraseis Inc., Denver, CO 80202, USA*

Accepted 2013 December 9. Received 2013 October 10; in original form 2013 June 28

## SUMMARY

Using formulae for both tensile and shear sources, we investigate spectral characteristics of microearthquakes induced by hydraulic fracturing, with application to passive-seismic data recorded during a multistage treatment programme in western Canada. For small moment magnitudes ( $M_w < 0$ ), reliable determination of corner frequency requires accurate knowledge of  $Q_p$  and  $Q_s$ , although spectral estimates of magnitude are relatively unaffected by uncertainty in seismic attenuation. Here, we estimate  $Q_p$  and  $Q_s$  using spectral ratios derived from perforation shots. Of the microseismic events analysed during the hydraulic-fracture treatment, 17 of 20 exhibit an  $S/P$  spectral ratio  $< 5$ , which is consistent with tensile failure. In addition, four microseismic events are characterized by a modulating source spectrum containing quasi-periodic notches. We interpret this spectral character to reflect a complex rupture pattern that involves rapid (5–8 ms) opening and closing of tensile cracks. In general, for tensile rupture on a penny-shaped crack, our model predicts that source radius ( $a$ ) is related to moment magnitude ( $M_w$ ) and internal fluid pressure within the fracture ( $P_i$ ) by a simple empirical scaling relation:  $\log_{10}(a) = [9 - \log_{10} 2]/3 + 0.5M_w - \log_{10}(P_i)/3$ .

**Key words:** Downhole methods; Seismicity and tectonics; Computational seismology.

## INTRODUCTION

Non-double-couple (non-DC) events, particularly tensile rupture, play an important role in rock deformation that occurs during hydraulic fracturing (Vavrycuk 2001; Šílený *et al.* 2009; Baig & Urbancic 2010; Warpinski & Du 2010; Song & Toksöz 2011). For example, based on experimental observations and small-scale field tests, Majer & Doe (1986) identified tensile events based on  $P$ -wave first motions; they found that tensile events are characterized by spectra with a rapid decay in high frequency, whereas shear sources are characterized by a broader spectra and a lower decay. Observations of non-DC earthquakes in volcanic and geothermal regions may provide potential natural analogues for tensile events observed during hydraulic fracturing (e.g. Shimizu *et al.* 1987). Using 70 well-recorded earthquakes from the Hengill–Grensdalur volcanic complex, Iceland, Miller *et al.* (1998) showed that  $\sim 75$  per cent of the events have significant non-DC mechanisms. Considerable source complexity was documented in their study including evidence for transtensional failure (i.e. near-simultaneous shear and tensile failure) that was interpreted to be indicative of fluid flow into newly formed cracks. Data from a dense portable seismograph network were used by Foulger *et al.* (2004) to determine moment tensors for 26 microearthquakes ( $0.4 \leq M \leq 3.1$ ) at Long Valley caldera, California. A variety of non-DC mechanisms were

obtained by inverting  $P$ - and  $S$ -wave polarities and amplitude ratios, most simply explained by a combination of shear and tensile failure in a volume-compensating process.

Spatial dimensions of microearthquake sources are encoded in spectral characteristics of the radiated seismic waves. Models for shear slip on a circular crack (Brune 1970, 1971; Madariaga 1976) predict the shape of source spectra and provide scaling relationships between spectral parameters (corner frequency and low-frequency plateau) and source parameters (source radius, stress drop and seismic moment). These source attributes complement those derived from moment-tensor analysis and are less affected by small effective apertures of receiver arrays that are typical for microseismic surveys (Eaton & Forouhideh 2011). Moreover, constraints on rupture characteristics derived from spectral analysis of radiated seismic waves may provide additional insights for geomechanical analysis of induced microseismicity (Goertz-Allmann *et al.* 2010).

Walter & Brune (1993) developed a model for far-field source spectra for tensile rupture, and compared these with modelled far-field spectra for shear-slip events. They showed that anomalously high  $P/S$  spectral amplitude ratios are diagnostic of tensile rupture. Their spectral models include several auxiliary parameters, namely seismic efficiency (the ratio of radiated seismic energy to total energy of deformation including aseismic processes that consume energy) and the ratio of  $P/S$  corner frequencies, which they suggest

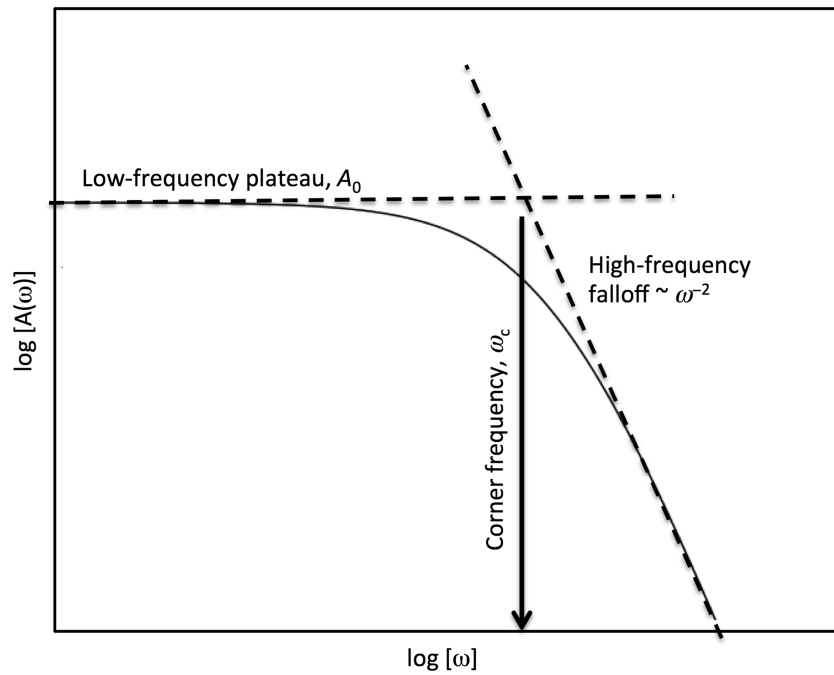


**Figure 1.** Relationship of Brune-model parameters to idealized far-field displacement spectrum for slip or tensile opening on a penny-shaped crack.

is linked to source rupture velocity. Walter & Brune (1993) also considered the spectral effects of rapid opening/closing of a tensile fracture, which we incorporate into our analysis.

The purpose of this study is to investigate spectral characteristics of microseisms induced by hydraulic fracturing and to explore the applicability of the spectral model for tensile rupture introduced by Walter & Brune (1993). To test these concepts, we consider waveform examples of 20 microseismic events acquired during a hydraulic-fracture stimulation of a tight gas reservoir in northeastern British Columbia, Canada. We emphasize, in particular, the importance of seismic quality factor ( $Q$ ) compensation for reliable estimation of spectral source parameters for microseismic data. Perforation-shot recordings are used here to estimate attenuation parameters ( $Q_P$  and  $Q_S$ ) using the spectral-ratio method. Finally, we show that the existence of notches in the radiated spectrum provides evidence for opening/closing of tensile cracks.

## THEORY

### Source spectra

Far-field body wave spectra from a seismic dislocation on a small circular crack can be represented using the Brune source model (Brune 1970, 1971). This theory has been extended and discussed by many others (e.g. Hanks & Wyss 1972; Randall 1973; Sato & Hirasawa 1973; Madariaga 1976, 1977). Here, we use the spectral model of Walter & Brune (1993), extended to include the effects of attenuation. In this formalism, the assumed idealized source model is represented using the ansatz (Brune 1970, 1971)

$$|\Omega^v(\omega, r)| = \frac{A_0^v(r) \exp(-\alpha_v r)}{1 + (\omega/\omega_c^v)^2}, \quad (1)$$

where  $v$  denotes wave type ( $P$  or  $S$ ),  $\omega$  is angular frequency,  $A_0$  is the low-frequency asymptotic limit of the displacement amplitude (Fig. 1) averaged over the unit sphere and  $r$  is source–receiver

distance. In addition,  $\alpha$  is an attenuation coefficient given by (e.g. Tonn 1991)

$$\alpha_v(\omega) = \frac{\omega}{2c_v Q_v}, \quad (2)$$

where  $c_v$  denotes  $P$ - or  $S$ -wave medium velocity ( $V_P$  or  $V_S$ ) and  $Q_v$  denotes seismic quality factor, here assumed to be independent of frequency. For the case of shear slip on a crack, the parameters  $A_0$  and  $\omega_c$  are given by

$$A_0^S = R_S \frac{4\sigma_2 a^3}{7\pi\rho V_S^3 r}, \quad \omega_c^S = \left( \frac{2835\pi\eta}{8\sqrt{3}\zeta^3 + 324} \right)^{\frac{1}{3}} \frac{V_S}{a} \quad (3)$$

for radiated  $S$  waves, and

$$A_0^P = R_P \frac{4\sigma_2 a^3}{7\pi\rho V_P^3 r}, \quad \omega_c^P = \zeta \omega_c^S \quad (4)$$

for radiated  $P$  waves. In eqs (3) and (4),  $R_v$  denotes the spherically averaged point-source radiation patterns for a shear crack (Fig. 2), given by  $R_S \approx 0.63$  and  $R_P \approx 0.52$  (Boore & Boatwright 1984). In addition,  $\sigma_2$  is shear stress acting on the crack,  $a$  is the radius of the spherical crack,  $r$  ( $\gg a$ ) is distance from the midpoint of the crack and  $\rho$  denotes mass density in the surrounding material. The term  $\zeta$  was introduced by Walter & Brune (1993) to represent the ratio of  $P$ - and  $S$ -wave corner frequencies. It should be noted that the lower limit for  $\zeta$  is 1, and the upper limit is equal to the velocity ratio  $V_P/V_S$  that characterizes the source region, assumed here to be 1.73. Finally,  $\eta$  denotes seismic efficiency, that is, the fraction of elastic energy that goes into seismic radiation. For the case of a tensile crack opening in response to an internal fluid pressure  $P_1$ , the parameters  $A_0$  and  $\omega_c$  are expressed in a similar manner (Walter & Brune 1993):

$$A_0^S = \sqrt{\frac{8}{15}} \frac{P_1 a^3}{2\pi\rho V_S^3 r}, \quad \omega_c^S = \left( \frac{1620\pi\eta}{47\sqrt{3}\zeta^3 + 216} \right)^{\frac{1}{3}} \frac{V_S}{a} \quad (5)$$

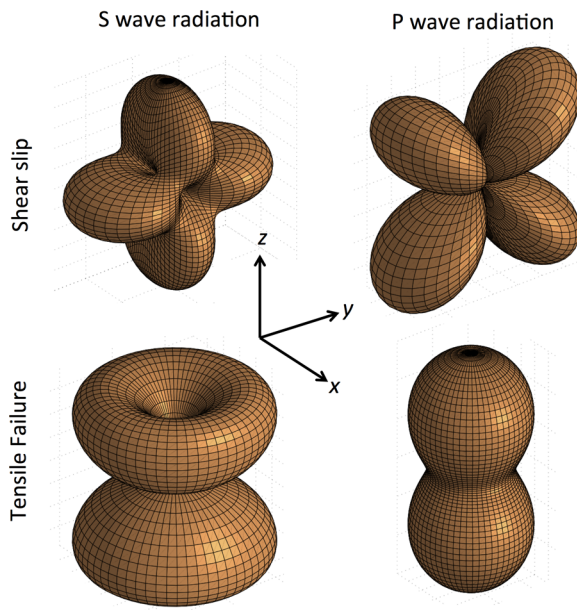


**Figure 2.** Amplitude radiation patterns for shear slip and tensile failure on a penny-shaped crack oriented within the  $x$ - $y$  plane and centred at the origin. Shear slip occurs in the  $+y$ -direction within the  $x$ - $y$  plane. Tensile failure opening occurs in the  $+z$ -direction. In the case of shear slip, the spherically averaged normalized radiated amplitudes are approximately 0.63 and 0.52 for  $S$ - and  $P$ -waves, respectively (Boore & Boatwright 1984). In the case of tensile failure, spherically averaged amplitudes are  $(8/15)^{1/2}$  and  $(47/15)^{1/2}$  for  $S$  and  $P$  waves, respectively (Walter & Brune 1993).

for radiated  $S$  waves, and

$$A_0^P = \sqrt{\frac{47}{15} \frac{P_1 a^3}{2\pi\rho V_p^3 r}}, \quad \omega_c^P = \zeta \omega_c^S \quad (6)$$

for radiated  $P$  waves. In this case, the spherically averaged point-source radiation patterns for a tensile crack are given by  $(8/15)^{1/2}$  and  $(47/15)^{1/2}$  for  $S$  and  $P$  waves, respectively (Walter & Brune 1993).

In all of these expressions, the elastic modulus  $\lambda$  has been eliminated for the sake of simplicity, under the assumption that the moduli  $\mu$  and  $\lambda$  are equal (i.e. the medium has a Poisson's ratio of 1/4). The reader is referred to Walter & Brune (1993) for a derivation of eqs (3)–(6), which are based on application of physical constraints to an idealized spectral model that explicitly avoids specifying details of the rupture process. This spectral model satisfies the basic conditions that low-frequency spectrum is asymptotic to a value that is proportional to the seismic moment and that radiated seismic energy is finite, which requires that spectral amplitudes fall off at a rate  $\geq \omega^{-1.5}$  (Walter & Brune 1993).

In practice, if far-field amplitudes and polarities of  $P$  and  $S$  waves are measured with sufficient sampling of the focal sphere (Eaton & Forouhdeh 2011) then shear and tensile events can be distinguished on the basis of the estimated moment tensor (or equivalently, estimated radiation patterns). In cases where the survey geometry does not provide sufficient sampling of the focal sphere, useful constraints on source mechanism may nevertheless be extracted from the  $S/P$  amplitude ratio (Kisslinger 1980; Kisslinger *et al.* 1981; Julian & Foulger 1996). The use of  $S/P$  amplitude ratio is particularly well suited to investigations of source mechanism, since corrections for event magnitude, geometrical spreading, attenuation and site effects are largely implicit in this approach (Hardebeck & Shearer 2003).

Fig. 3 shows probability density for  $S/P$  amplitude ratio for both shear and tensile failure. For a random direction of propagation from the source, the  $S/P$  amplitude ratio for shear events is expected to be greater than 5 at  $\sim 90$  per cent level of confidence. Conversely, for tensile events the  $S/P$  amplitude ratio is less than 4.671 for any direction. On this basis, we suggest the use of an  $S/P$  amplitude ratio  $< 5$  as an approximate measure to discriminate between shear and tensile events. For these two types of sources, this discriminant does not require *a priori* knowledge of the precise source mechanism.

Given measured values of  $A_0$ ,  $\omega_c$  and  $\zeta$  for  $P$  and  $S$  waves radiated from a microearthquake, together with *a priori* knowledge of  $\rho$ ,  $V_P$ ,  $V_S$  and  $r$ , it is possible to estimate several basic source parameters. For example, the seismic moment is given by (see Appendix A)

$$M_0 = \frac{4\pi\rho c_v^3 |A_0^v| r}{R_v}, \quad (7)$$

where  $|A_0^v|$  denotes the measured low-frequency plateau amplitude ( $v = P$  or  $S$ ). Although strictly speaking,  $R_v$  depends on the type of source, in practice the differences are generally small ( $< 0.05$  magnitude units) between calculations that use tensile and shear formulae. In the absence of averaging using an array of receivers that completely surrounds the source, however, the radiated amplitudes for any given measurement will generally differ from  $R_v$ . As elaborated below, one consequence is that seismic moments estimated independently using  $P$  and  $S$  waves typically generally do not agree exactly.

Once seismic moment has been estimated, the moment magnitude can be determined using the empirical relation (e.g. Stein & Wysession 2009)

$$M_W = \frac{2}{3} \log_{10} M_0 - 6. \quad (8)$$

Earthquakes are almost always regarded as pure-shear (DC) sources, and various scaling relations have been used to estimate stress drop and source dimensions from measured  $S$ -wave corner frequencies and low-frequency plateau amplitude values. For example, based on eqs (3) and (5), it is clear that once the low-frequency plateau spectral values are determined, the products  $\sigma_2 a^3$  (or  $P_1 a^3$ ) can be estimated for shear (or tensile) events. Furthermore, if the seismic efficiency parameter ( $\eta$ ) is known, then the crack radius ( $a$ ) and applicable stress parameter can be computed. The parameter  $\eta$  is expected to vary over a wide range, however, rendering uncertain such spectral estimates of source dimensions and stress (*cf.* Beresnev 2001). Finally, Walter & Brune (1993) have noted that the ratio of  $P$ - and  $S$ -wave corner frequencies,  $\zeta$ , is linked to rupture velocity. For the hypothetical case of instantaneous rupture,  $\zeta$  is expected to approach the  $V_P/V_S$  velocity ratio, whereas in the asymptotic limit of slow rupture,  $\zeta$  is expected to approach unity.

Although it is standard practice to employ spherically averaged amplitude values ( $R_v$ ) to compute magnitude based on eqs (7) and (8), more accurate magnitude estimates can be obtained by moment-tensor inversion, since this approach accounts for the  $P$ - and  $S$ -wave radiation patterns. To illustrate the errors in magnitude that are introduced by the use of spherically averaged amplitude values, Fig. 4 shows normalized probability density for the magnitude error for shear and tensile events, based on  $S$ -wave amplitude radiation patterns and uniform sampling of the focal sphere. Similar characteristics apply to  $P$  waves. For both types of sources, this analysis indicates that magnitude errors that arise from the use of spherically averaged amplitude values rather than the correct directionally dependent amplitude generally fall within the range of  $-0.6$  to  $0.2$  magnitude units.

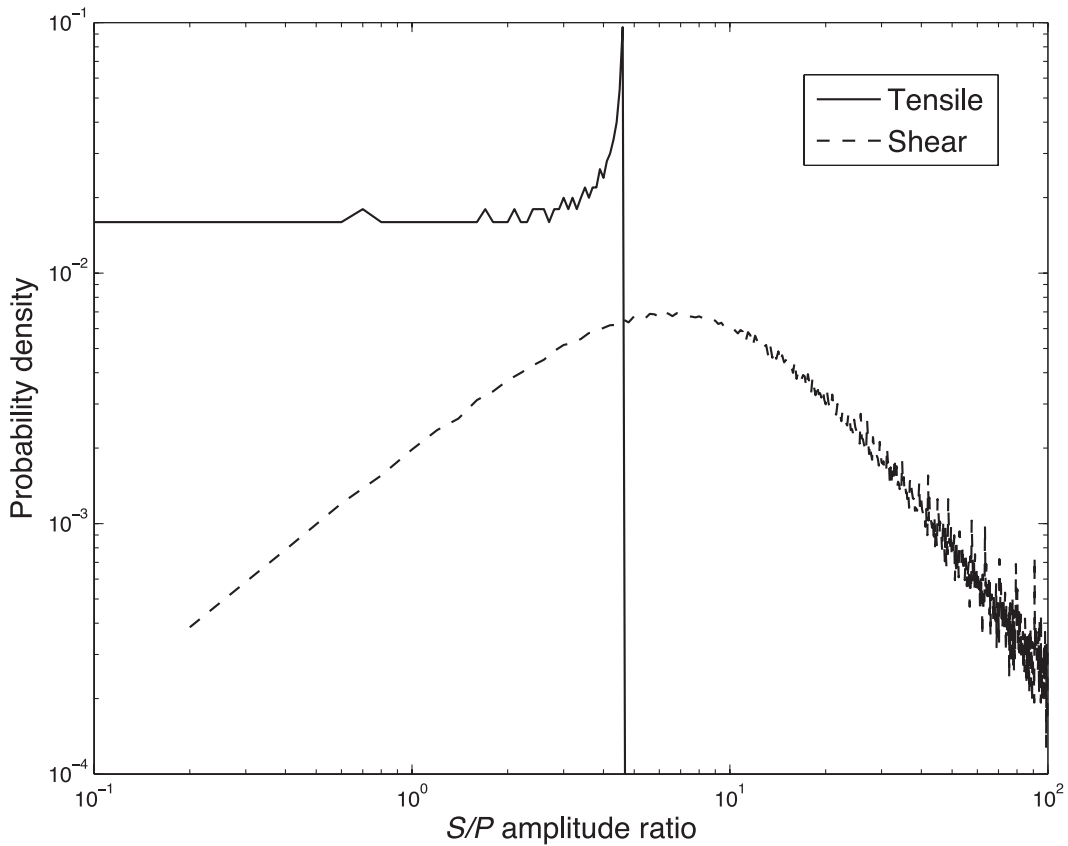


**Figure 3.** Normalized probability density for  $S/P$  amplitude ratio, based on uniform sampling of the focal sphere. For a random source–receiver direction, there is 9.1 per cent probability of  $S/P < 4.617$  for shear events, versus 100 per cent probability of  $S/P$  in this range for tensile rupture. See Appendix B for a description of the computation method used to generate these curves.

As shown in Appendix A, our source model for tensile failure leads to a simple empirical scaling relation for source radius

$$\log_{10}(a) = [9 - \log_{10} 2]/3 + 0.5Mw - \log_{10}(P_1)/3, \quad (9)$$

where  $a$  is expressed in metres and internal fluid pressure ( $P_1$ ) in Pa. In the case of microearthquakes induced by hydraulic fracturing, this relationship is particularly convenient, since the moment magnitude ( $Mw$ ) is routinely estimated using microseismic observations and  $P_1$  can be estimated from the hydraulic-fracture treatment data. Estimation of the source radius ( $a$ ) using this expression does not require measurement of the corner frequency, in contrast to the case for shear slip on a fault (Boore 1983).

The superposition of signals from events that are closely separated in space and time gives rise to complexity in the radiated source spectrum (e.g. Haddon & Adams 1997). In the special case of two collocated events of opposite polarity, separated by a small time interval  $\tau$ , the source spectrum can be computed easily by applying the filter (Walter & Brune 1993)

$$F(\omega) = 2 - 2 \cos(\omega\tau) \quad (10)$$

to the source spectrum given by eq. (1). This filter introduces a series of periodic notches in the source spectrum. Composite events of this type may arise due to fluid pressure changes in the case of rapid opening and closing of a tensile crack (Foulger & Long 1984; Foulger 1988).

### Q estimation

Hydraulic-fracture completions often make use of perforation (perf) shots, comprised of projectiles or shaped explosive charges used before each treatment stage to create holes in the well casing, in order to connect the interior of the wellbore with the surrounding medium. Since the location and approximate timing of perf shots are known, they can be used for calibration of microseismic systems. Here, waveforms recorded from perf shots are used to estimate the quality factor ( $Q$ ) for  $P$  and  $S$  arrivals.

We begin by expressing the spectrum  $A_{ij}(\omega)$  of the  $i$ th perf shot recorded on the  $j$ th receiver as

$$A_{ij}(\omega) = S_i(\omega)\Omega_{ij}(\omega) \exp\left(-\frac{|\omega|r_{ij}}{2cQ}\right), \quad (11)$$

where  $S_i$  denotes the spectrum of the source,  $\Omega_{ij}$  is a part of the Green's function for the medium that embodies the frequency-dependent path effects and  $r$  is the source–receiver distance. Since all perf shots for a given treatment programme have virtually identical source characteristics, the far-field spectra of the  $i$ th and  $j$ th perf shots are assumed to be related by a frequency-independent scalar  $\xi_{ij}$  such that

$$S_i(\omega) = \xi_{ij}S_j(\omega), \quad \text{no summation over } j, \quad (12)$$

where  $\xi_{ij}$  incorporates location-dependent coupling of the perf shot with the surrounding medium, as well as any directional dependence of the radiated waves.

We use the spectral-ratio method for  $Q$  estimation, since it provides a relatively robust and flexible procedure (Tonn 1991).

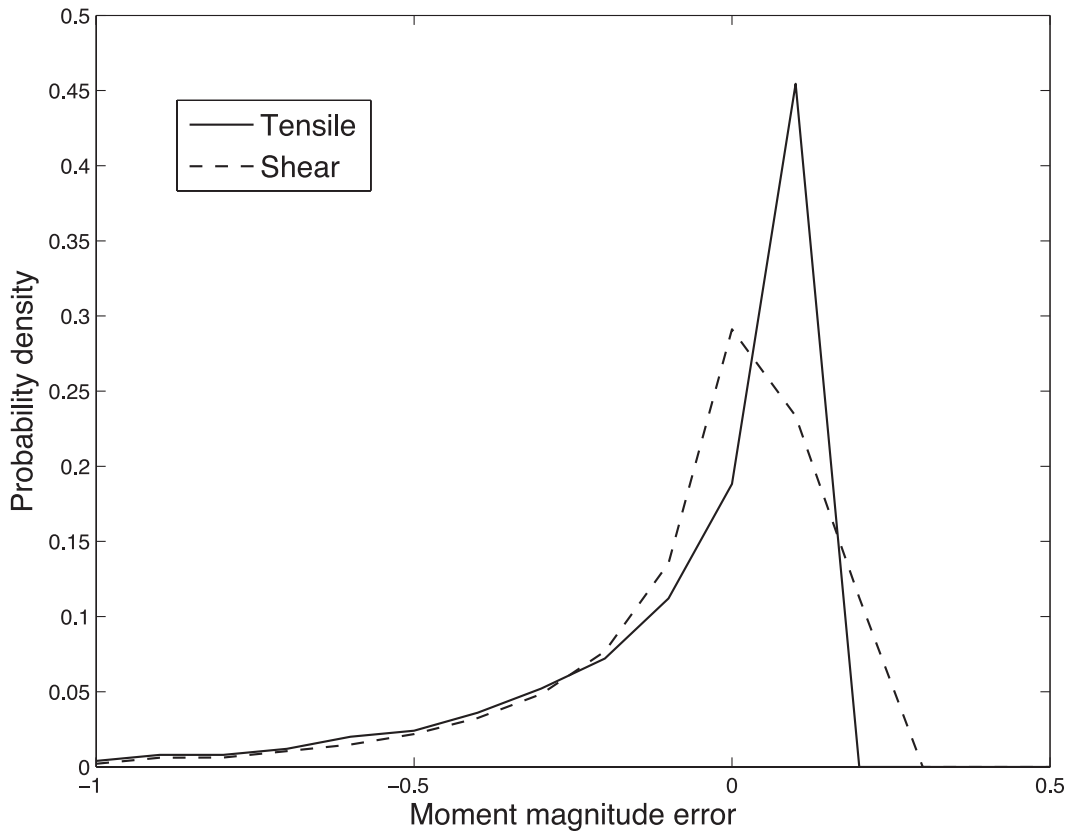


**Figure 4.** Normalized probability density for magnitude error arising from the use of spherically averaged  $S$ -wave amplitude. The calculation is based on uniform sampling of the focal sphere. See Appendix B for a description of the computation method used to generate these curves.

Typically, this method is applied using multiple receiver locations acquired at various distances from a common source; in this study, however, we use data recorded from different perf shots. In order to minimize spectral distortions associated with different paths and azimuths, we confine our measurements of  $Q$  to pairs of perf shots that share a common azimuth. We then assume that the path effect can be adequately approximated by frequency-independent geometrical spreading, that is,  $\Omega_{ij}(\omega) \sim G_{ij}$ .

Given these assumptions, for a given arrival ( $P$  or  $S$ ) recorded from two different perf shots, the ratio of spectral amplitudes is given by

$$\frac{|A_2(\omega)|}{|A_1(\omega)|} = \frac{\xi G_2}{G_1} \exp\left(-\frac{|\omega|(r_2 - r_1)}{2cQ}\right), \quad (13)$$

where the  $ij$  subscripts have been replaced with a single index for ease of notation. This relationship implies that a semi-logarithmic plot of the ratio of the amplitude spectrum of the distal perf shot normalized by the amplitude spectrum of the proximal perf shot will have a slope given by  $\pi(r_2 - r_1)(cQ)^{-1}$ , from which  $Q$  can be readily determined. In practice, a windowing function is applied to isolate distinct  $P$  and  $S$  arrivals, enabling independent estimation of  $Q_P$  and  $Q_S$ .

### SENSITIVITY TO NOISE AND $Q$

To illustrate sensitivity to noise level and  $Q$  uncertainty, numerical calculations of far-field  $S$ -wave source spectra are presented in Fig. 5. These calculations are based on eqs (1), (2), (5) and (6) for representative tensile events. Model parameters and calculated values are summarized in Table 1. For the hypocentral distance

( $r = 500$  m) and range in  $Q$  ( $50 \leq Q \leq 200$ ) considered in these calculations, the effects of attenuation are dramatic. In particular, the high-frequency fall-off of the modelled source spectra tends to be dominated by attenuation and is significantly greater than the elastic limit of  $\omega^{-2}$ . This implies that, for this observation distance and degree of anelastic attenuation, determination of corner frequency requires accurate knowledge of  $Q$ . We remark that near-field source terms, which contribute significantly to ground motion within a few wavelengths of the source (e.g. Atkinson *et al.* 2008), are neglected for the curves plotted in Fig. 5. Thus, for frequencies less than  $\sim 20$  Hz these model spectra may not be representative of observed event spectra. In practice, spectral measurements of microseismic events are confined to higher frequencies where the far-field assumption is valid.

Fig. 6 illustrates the sensitivity of magnitude and corner-frequency estimates to white noise and  $Q$  uncertainty. Model parameters for these tests are summarized in Tables 2 and 3. In Fig. 6(a), the reference  $S$ -wave model spectrum contains no noise and is computed for  $Q_S = 150$ . The dashed curves show best-fitting model spectra, calculated using eqs (1) and (2) based on *a priori* assumptions of no attenuation ( $Q_S \rightarrow \infty$ ),  $Q_S$  too high (200) and  $Q_S$  too low (100). The best-fitting curves were obtained by minimizing the misfit between model and reference spectra based on a least-squares criterion. Specifically, an exhaustive search procedure was used to select the parameter  $A_0$  in order to minimize the least-squares misfit within a user-defined low-frequency band (50–100 Hz), followed by an exhaustive search to select  $\omega_c$  to minimize misfit in a user-defined high-frequency band (400–700 Hz). Although most curve fits appear reasonable, derived misfits in corner frequency are large (Table 2). In general, if *a priori* estimate of  $Q$  exceeds the correct

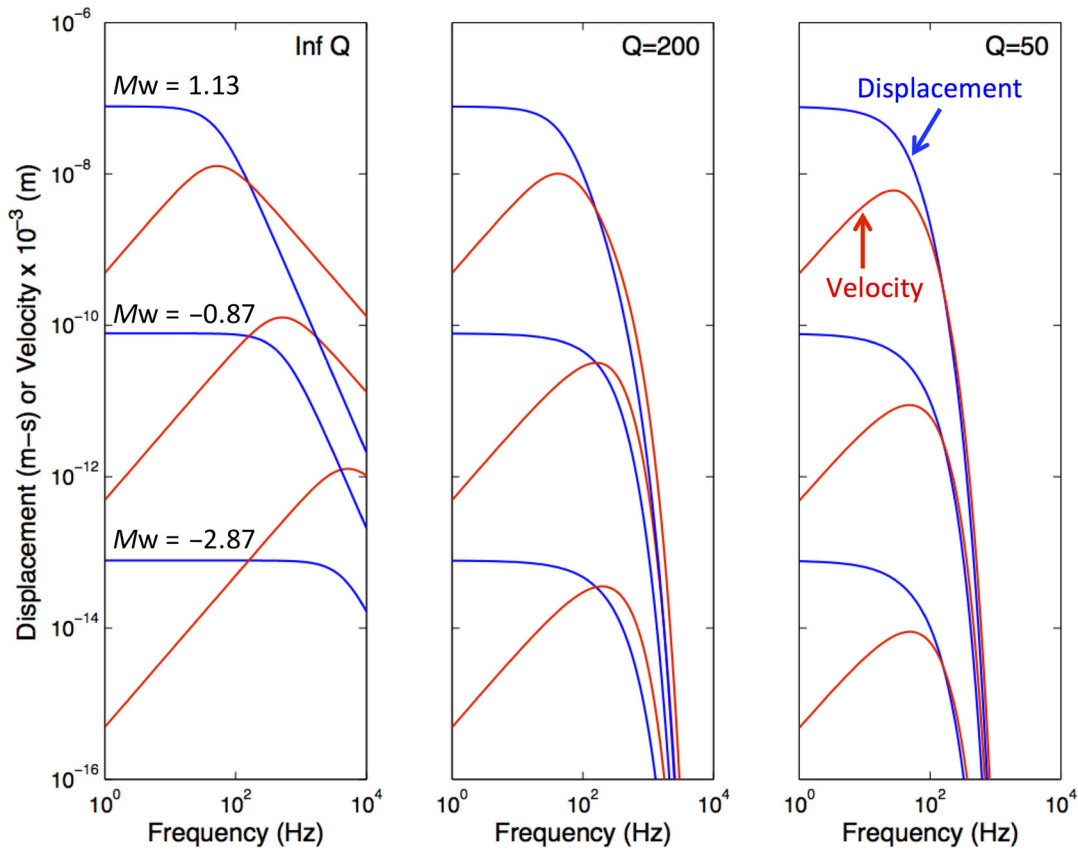


**Figure 5.** Model spectra for models with crack radius  $a = 0.1, 1.0$  and  $10.0$  m ( $M_w = -2.87, -0.87$  and  $1.13$ ; see Table 1). Increasing attenuation (decreasing  $Q$ ) has a profound effect on the high-frequency slopes of the source spectra.

**Table 1.** Parameters for representative tensile  $S$ -wave source spectra.

Model	Crack radius, $a$ (m)	$M_w$	Corner frequency, $f_c$ (Hz)
1	0.1	-2.87	5182
2	1.0	-0.87	518
3	10.0	1.13	51.8

Note: Medium parameters for all models:  $V_S = 3100$  m s<sup>-1</sup>,  $\rho = 2500$  kg m<sup>-3</sup>,  $\eta = 0.1$ ,  $r = 500$  m,  $P_i = 50$  MPa.

value, the inferred corner frequency will be too low; conversely, if *a priori* estimate of  $Q$  is less than the correct value, the inferred corner frequency will be too high. As expected, uncertainties in  $Q$  have relatively little effect on the estimation of magnitude, which is estimated from the low-frequency displacement asymptote and does not depend on the corner frequency.

To consider the effects of noise, a series of tests was conducted based on a modified spectral model

$$|\Omega^v(\omega, r)| = \frac{A_0^v(r) \exp(-\alpha_v r)}{1 + (\omega/\omega_c)^2} + \frac{N_0}{i\omega}, \quad (14)$$

which differs from eq. (1) only by the inclusion of an additive noise parameter,  $N_0$  to model constant background noise in the velocity spectrum. Parameters for the noise sensitivity tests are summarized in Table 3. Using the same least-squares fitting approach described above, model parameters  $A_0$  and  $\omega_c$  were obtained using an exhaustive search procedure, based on prescribed values of  $Q$  and  $N_0$ . Comparing Tables 2 and 3, we find that a factor of two uncertainty in noise has a less dramatic effect on inferred magnitudes and corner frequencies than a similar uncertainty in  $Q$ . Identical inferences can be derived for source-parameter estimation using  $P$  waves.

## FIELD EXAMPLE

Spectra for shear and tensile sources are used here to investigate source characteristics for a microseismic field experiment acquired in 2011 August in northwest Canada (Eaton *et al.* 2013). In this field data example, multistage hydraulic-fracture treatments in two horizontal wells at a depth of  $\sim 1950$  m were recorded using both surface and borehole sensors (Fig. 7). In this study, our analysis is confined to data from the borehole sensors, as relatively few events were detected at the surface. The borehole toolstring was deployed in a deviated well in a depth range of 1670–1830 m. The toolstring consisted of a six-level array of 4.5 Hz geophones with downhole digitization. Background velocities at the reservoir level are  $V_p \sim 5$  km s<sup>-1</sup> and  $V_s \sim 3$  km s<sup>-1</sup>. Most perforation shots were well recorded to distances of about 2 km. These signals were used to estimate  $Q_p$  and  $Q_s$ . In addition, numerous high-frequency ( $> 100$  Hz) microseismic events with moment magnitudes ranging from  $-2.3$  to  $-0.3$  were detected to distances of up to 1.5 km.

### $Q$ analysis

Several examples of perf shots are shown in Fig. 8. The effects of attenuation are expressed as a reduction in amplitude coupled with relative loss of high-frequency content at greater observation distance. Signal and noise spectra were computed by windowing the desired waveform and pre-event noise. Pairs of perf shots were selected for  $Q$  determination based on similarity in ray azimuth for the distal and proximal perf shot locations (Fig. 9). As illustrated in Fig. 10,  $Q_p$  and  $Q_s$  values were determined using the spectral-ratio method described above. The spectra were computed by taking the

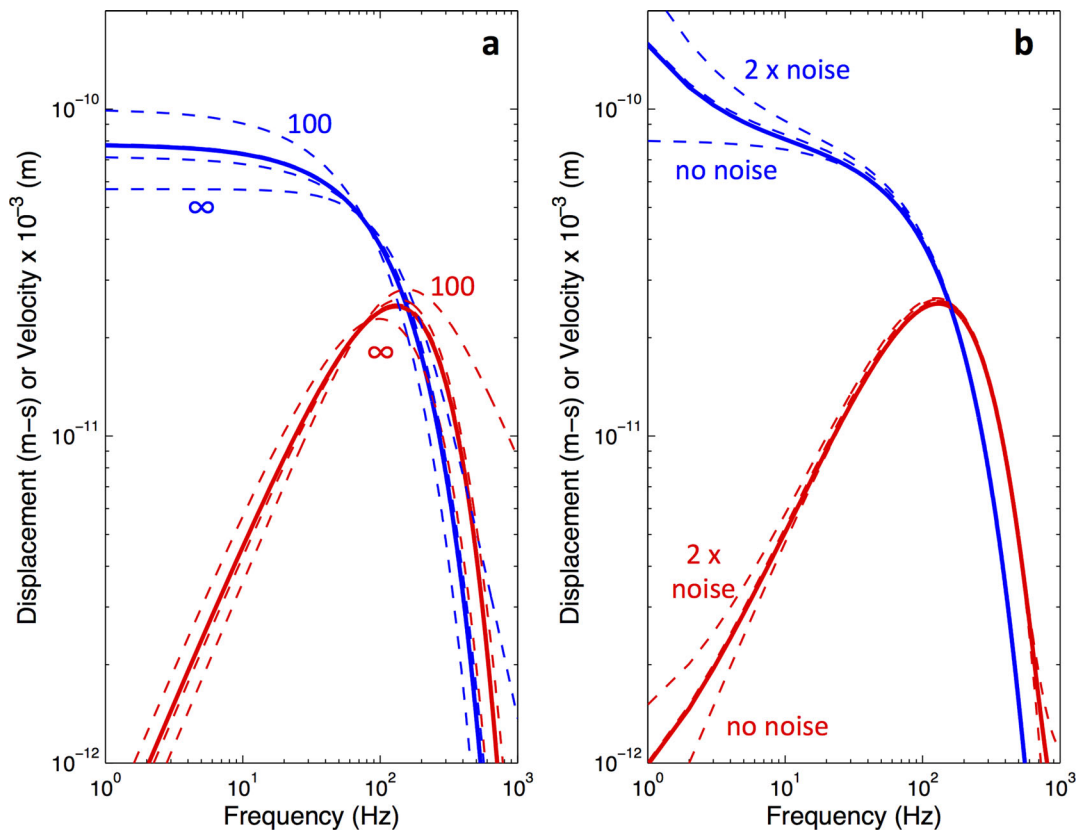


**Figure 6.** Model fits for tests of (a)  $Q$  sensitivity and (b) noise sensitivity. Model parameters are given in Tables 2 and 3, respectively. Blue = displacement spectrum; red = velocity spectrum. Solid curves: no noise, correct  $Q_S = 150$ . Dashed curves show best-fitting model spectra for the cases of no attenuation ( $Q_S \rightarrow \infty$ ),  $Q_S$  too high (200) and  $Q_S$  too low (100).

**Table 2.** Inversion tests for  $Q$  sensitivity (no noise).

$Q$ value used for inversion	Estimated $f_c$ (Hz)	Estimated $Mw$ – true $Mw$
$\infty$	157	–0.09
200	326	–0.03
150	544	0.002
100	$\infty$	0.07

*Notes:* Parameter values to generate noise-free tensile  $S$ -wave source spectrum:  $V_S = 3100 \text{ m s}^{-1}$ ,  $\rho = 2500 \text{ kg m}^{-3}$ ,  $\eta = 0.1$ ,  $Q = 150$ ,  $r = 500 \text{ m}$ ,  $P_1 = 50 \text{ MPa}$ ,  $a = 1.0 \text{ m}$  ( $Mw = -0.87$ ). Correct value of  $f_c$  is 534 Hz. Source parameters are estimated for a low-frequency plateau in the range  $50 < f < 100 \text{ Hz}$ .

**Table 3.** Inversion tests for noise sensitivity (correct  $Q$  used).

Uniform noise level $N_0$ (m)	Estimated $f_c$ (Hz)	Estimated $Mw$ – true $Mw$
$1 \times 10^{-9}$	438	0.01
$5 \times 10^{-10}$	490	0.01
0	553	0.01

*Notes:* Event parameter values to generate tensile  $S$ -wave source spectrum: white noise level in velocity spectrum =  $5 \times 10^{10} \text{ m}$ ,  $V_S = 3100 \text{ m s}^{-1}$ ,  $\rho = 2500 \text{ kg m}^{-3}$ ,  $\eta = 0.1$ ,  $Q = 150$ ,  $r = 500 \text{ m}$ ,  $P_1 = 50 \text{ MPa}$  ( $Mw = -0.87$ ). Correct value of  $f_c$  is 534 Hz. Source parameters are estimated for a low-frequency plateau in the range  $50 < f < 100 \text{ Hz}$ .

Fourier transform, after isolating signals from  $P$ - and  $S$ -wave direct arrivals by applying a Gaussian windowing function with a standard deviation of 75 ms. The application of this windowing function has the effect of smoothing the computed spectrum, without affecting the overall amplitudes.

Using all of the available high-quality perf-shot recordings, we found significant scatter in the results; we obtained average values of  $Q_P = 109$  ( $N = 24$ ) and  $Q_S = 101$  ( $N = 16$ ) with standard deviations of 49 and 46, respectively (see Supporting Information for complete results). These average  $Q$  values are used in the spectral calculations below, with the caveat that large scatter in  $Q$  estimates imply significant uncertainties in corner frequency.

### Source analysis

A subset of 20 events from the complete set of detected events was selected for further analysis, based on good signal to noise (S/N) and the discernibility of distinct  $P$  and  $S$  arrivals. Several examples of seismograms with corresponding spectrograms and amplitude spectra are presented in Fig. 11. The sample stage 1 event is located  $\sim 358 \text{ m}$  from the monitor well. The  $P$ -wave arrival is not visible (due to the plot scale, which is dominated by the  $S$  wave) in the seismogram, but it can be discerned in the spectrogram based on abrupt change in frequency content from the background levels. The  $S$ -wave arrival has high signal level to the Nyquist frequency (1000 Hz). The spectrum is dominated by the  $S$  wave and has good S/N  $> 20 \text{ dB}$  in the frequency range  $100 < f < 1000 \text{ Hz}$ . The sample stage 3 event is located  $\sim 456 \text{ m}$  from the geophone. Both  $P$  and  $S$  arrivals are clearly visible in the raw seismogram, and the spectrum has S/N  $\sim 20 \text{ dB}$  in the range  $100 < f < 350 \text{ Hz}$ .

Brune source parameters for the analysed events were computed using a procedure similar to Abercrombie (1995). The overall workflow can be summarized as follows:

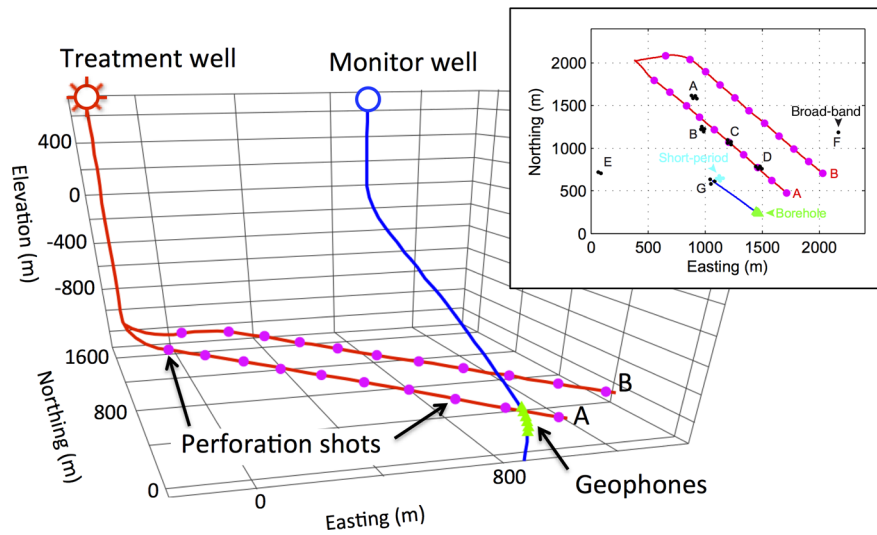


**Figure 7.** Field layout for the microseismic monitoring survey in western Canada. Inset shows a map view of the survey, including surface broad-band sensors (installed in miniarrays denoted A–G) and a 12-channel 15 Hz geophone (short period) array.

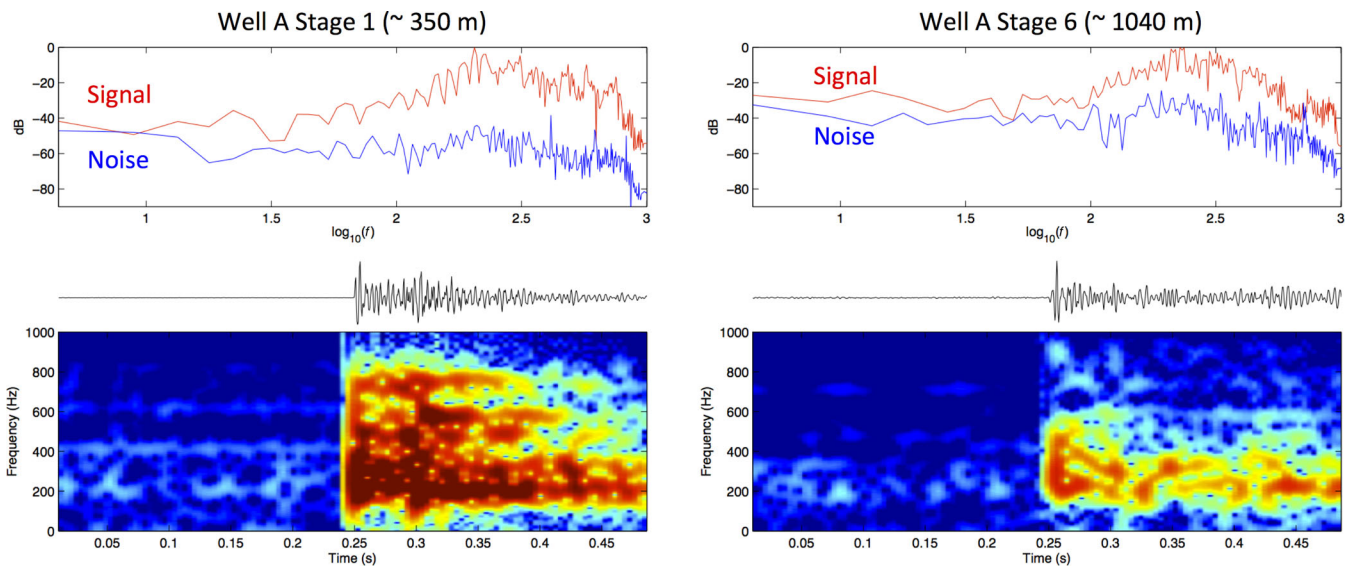


**Figure 8.** Examples of two perforation shots, used here to estimate  $Q$ . Top panel shows calculated signal and noise spectra. Middle panels show observed seismograms (vertical component). Lower panels show spectrograms, dominated by the  $P$  arrival. Note the reduced amplitudes and relative loss of high frequencies with increasing distance from stage 1 (350 m) to stage 6 (1040 m). Precise time synchronization for the perforation shots was not available, so the start time of the trace is not exactly the event time.

(1) For each event, the three-component geophone with the highest S/N is selected and used to pick  $P$ - and  $S$ -wave arrival times.  $P$  and  $S$  amplitudes are estimated using the maximum vector amplitude within two dominant periods following the picked arrival time.

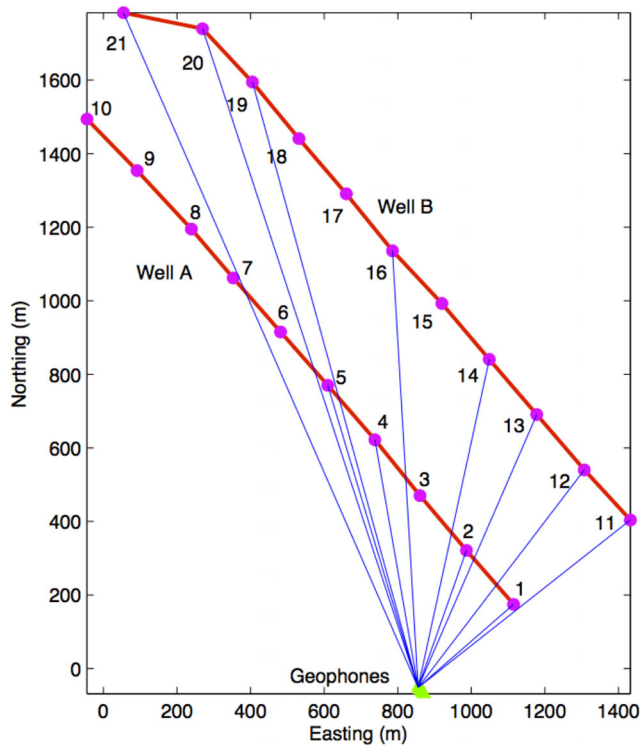
(2) A Gaussian windowing function with a standard deviation of 0.1 s is applied to isolate the desired arrival, as well as pre-event noise.

(3) For each component (east, north and vertical), velocity spectra for signal and noise are computed by taking the Fourier transform of the windowed trace, normalized such that absolute units are preserved. Displacement spectra for individual components are then computed by dividing velocity spectra by  $i\omega$ . Finally, scalar displacement spectra for signal and noise are calculated from the individual components based on the vector amplitude.

(4) An initial estimate of the low-frequency plateau is obtained by taking the difference between the average signal and noise amplitude within a user-defined frequency range (here 200–300 Hz was used).

(5) Corner frequency is determined by finding the optimum (least-squares) fit between observed and modelled displacement spectra, using an exhaustive search within the range  $0 < f_c < 10\,000$  Hz, where an obtained value of  $f_c = 10\,000$  Hz is interpreted as undefined. The modelled spectrum is computed using eq. (14), with fixed values of  $Q$  and  $N_0$ . Our method considers corner frequencies above the Nyquist frequency, since even at these higher values of corner frequency the effects on spectral shape remain significant.

(6) The low-frequency plateau amplitude ( $A_0$ ) is adjusted and step 6 is repeated, as necessary, until misfit (variance) converges to a minimum value. Adjustment in low-frequency plateau involves a modest increase or decrease ( $\pm 50$  per cent) to improve the fit of the modelled and observed spectrum.



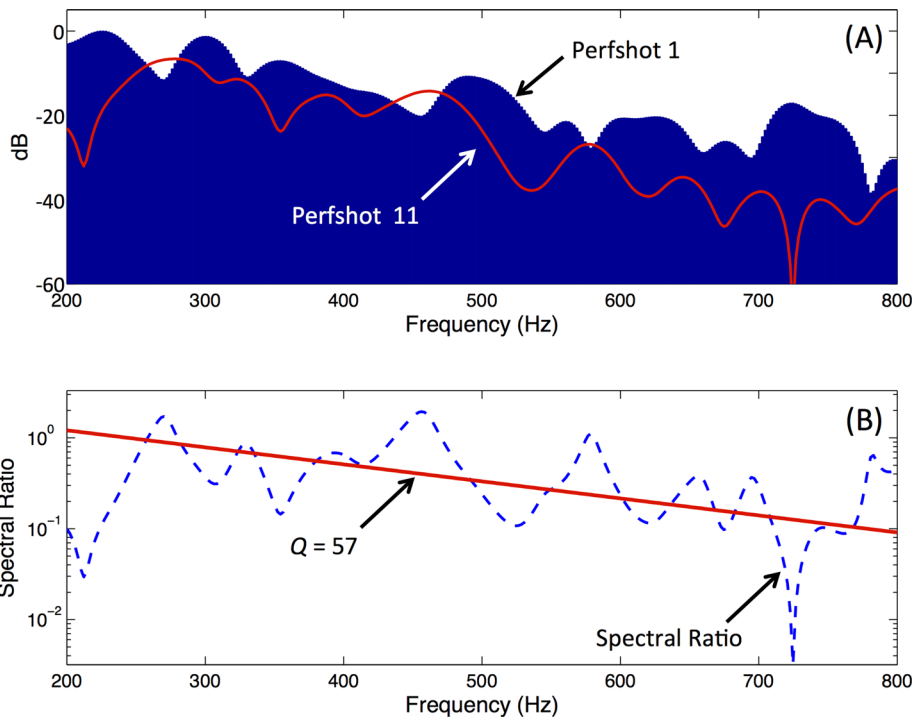
**Figure 9.** Ray paths from perforation shots to geophones, used for estimation of  $Q$ . Locations of perforation shots are numbered. Pairs of events are selected based on a near-common azimuth to the geophones.

Fig. 12 shows an example fit obtained using this procedure. Although erratic fluctuations are evident in the observed spectrum, the Brune model provides a good overall fit. The corner frequency in this case is undefined, meaning that the effects of

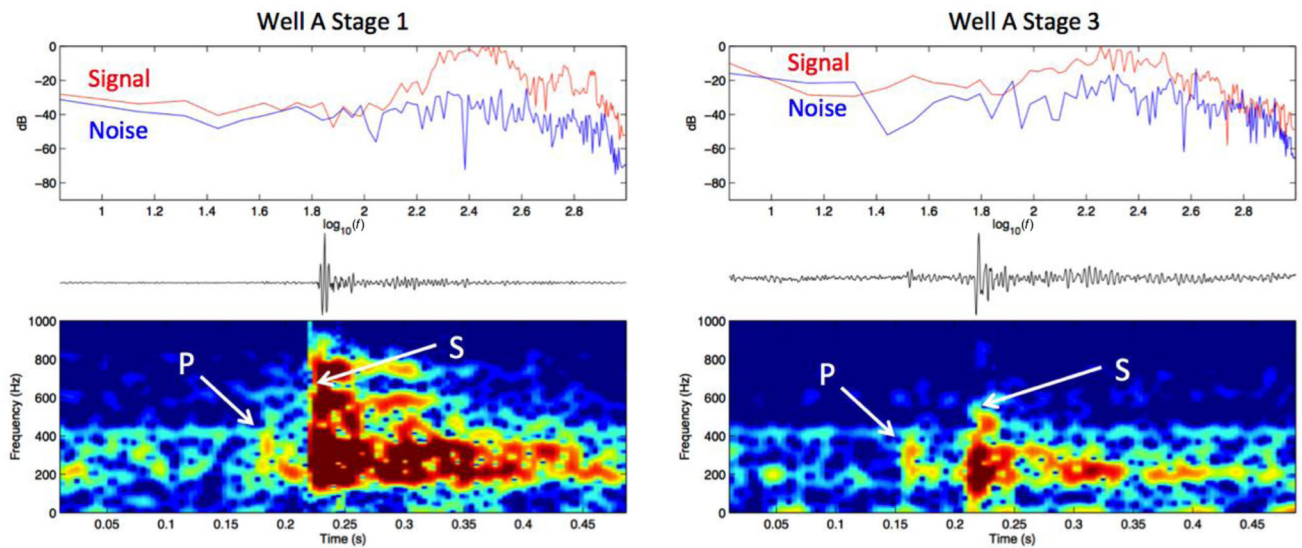
$Q$ , rather than  $\omega^{-2}$  fall-off, dominate the high-frequency spectral decay.

Table 4 summarizes inferred source parameters for the 20 analysed events. Observation distances sampled by this set of events span a range from  $\sim 250$  to  $\sim 1500$  m. Calculated moment magnitudes fall within the range  $-2.06 \leq M_w \leq -0.34$ ; this range likely reflects a sampling bias towards larger magnitudes, due to detection limits for this experiment (Eaton et al. 2013). As expected, based on uncertainty in  $Q$  from analysis of perf shots and background noise levels from the source analysis, inferred corner frequencies exhibit a high degree of scatter; where defined, they fall within the range  $207 \leq f_c \leq 1603$  Hz. Measured  $S/P$  amplitude ratios vary from 1.13 to 8.91. 17 of the 20 events have an  $S/P$  amplitude ratio less than 5, which we consider to be indicative of tensile failure. In addition, four of the analysed events show source spectra characterized by quasi-periodic amplitude modulation above and below the best-fitting Brune spectrum. Fig. 13 shows an example of this type of source spectrum, which may be indicative of a complex source model such as several closely spaced events (Haddon & Adams 1997). As shown in Table 4, this set of four events is generally characterized by low value of  $S/P$  amplitude ratio, suggesting that a component of tensile failure may exist.

For each of the four events with a complex source spectrum, we have performed a second analysis in which the filter defined by eq. (10) is applied the Brune source model. This represents a simplified model for rapid opening and closing of a tensile crack, defined by a time parameter  $\tau$  that specifies delay time between two events of equal moment and opposite polarity. To obtain a model fit, step 6 in the workflow outlined earlier was amended to include adjustment to  $\tau$ . As shown in Fig. 13, in this case this crack opening/closing model provides a better fit to the observed spectra than the conventional Brune model. We find an rms misfit of  $5.7 \times 10^{-13}$  ms for the opening/closing model, compared to  $8.4 \times 10^{-13}$  ms for



**Figure 10.** Example of spectral ratio calculation of  $Q$ . (a)  $P$ -wave spectra for perfshot 1 ( $r = 383$  m) and perfshot 11 ( $r = 783$  m). The  $P$ -wave arrivals have a very similar ray path from the closer source position (perfshot 1) to the geophone array. A Gaussian window has been applied to smooth the spectra. (b) Spectral ratio, showing calculated  $Q_p$  based on linear regression within the frequency range  $250 \text{ Hz} < f < 750 \text{ Hz}$ .



**Figure 11.** Examples of two microseismic events used for source analysis. Top panel shows calculated signal and noise spectra. Middle panels show observed seismograms (vertical component). Lower panels show spectrograms, which show easily discernible *P* and *S* arrivals.

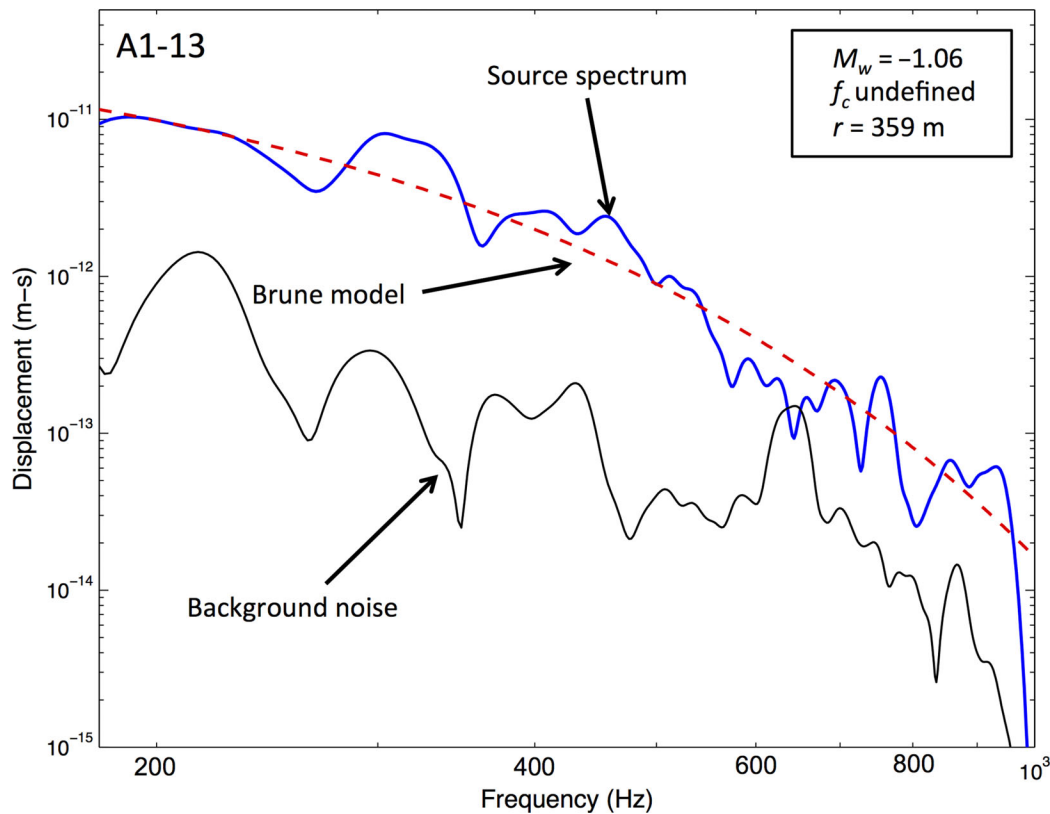


**Figure 12.** Example of source-spectrum model fitting for event A1-13. Blue curve shows the displacement spectrum for the *S*-wave arrival, after application of a Gaussian windowing function. Dashed red curve shows the best-fitting Brune source model, with parameters summarized in the inset box. Black curve shows background noise based on a pre-event noise window. Signal amplitude is above the noise level over the entire bandwidth investigated.

the standard Brune model (a variance reduction of 52.4 per cent). Table 5 provides a summary of results of this analysis for the four events with complex source spectra. Comparing parameters with the standard Brune model fit (Table 4), we find relatively small changes in  $M_w$  and a systematic tendency towards increasing  $f_c$ . Due to the relatively low values of  $S/P$  amplitude ratio for these four events, we have used *S*-wave amplitude coefficients for tensile rupture to compute  $M_w$ , rather than *S*-wave amplitude coefficients for shear

slip, as in the previous calculations. The inferred time delay between opening and closing varies in the range from 5.2 to 7.7 ms.

## DISCUSSION

Foulger & Long (1984) and Foulger (1988) have suggested that opening of a tensile crack, as characterized by predominantly

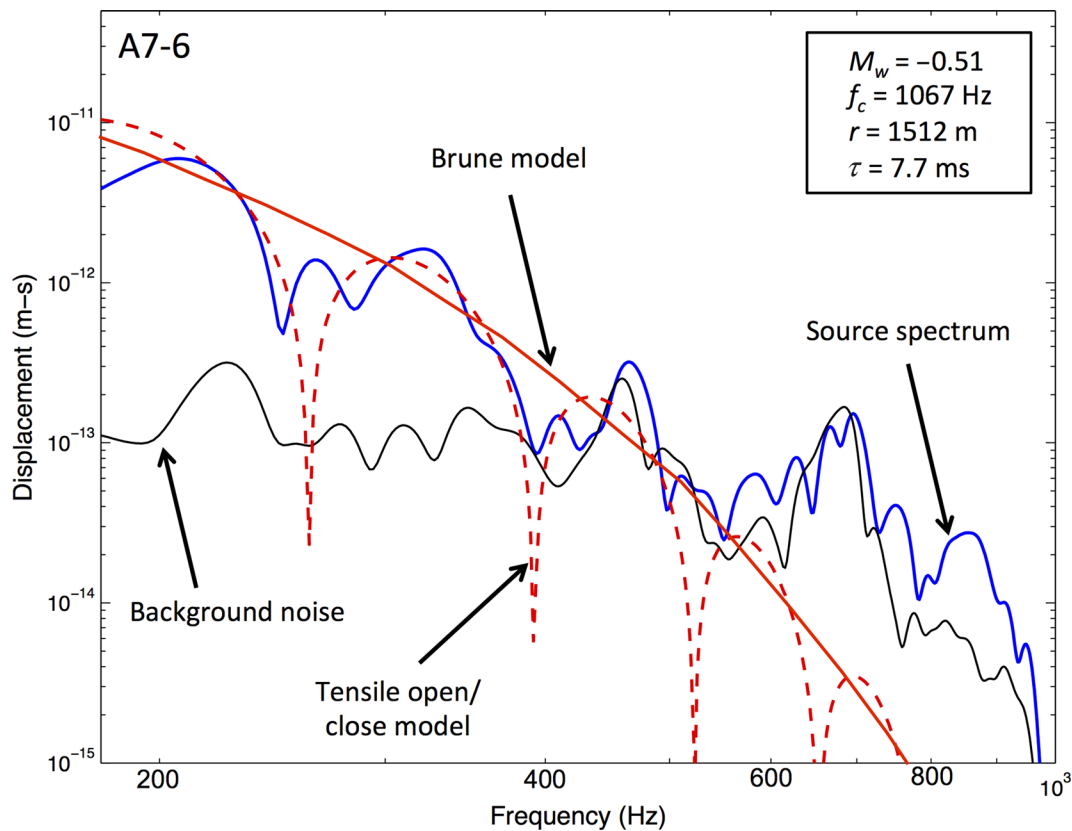


**Figure 13.** Example of source-spectrum model fitting for event A7-6, which is characterized by a complex spectral shape with amplitude modulation. Blue curve shows the displacement spectrum for the  $S$ -wave arrival, after application of a Gaussian windowing function. Dashed red curve shows the best-fitting tensile opening/closing model (see text), with parameters summarized in the inset box. Solid red curve shows the best-fitting standard Brune model. Black curve shows background noise based on a pre-event noise window. Signal amplitude is above the noise level from 150 to 500 Hz.

compressional first motion, may be followed by a pressure drop in the crack. This process is hypothesized to occur because fluid flow is not as fast as the fracture propagation, resulting in formation of a metastable crack opening (Julian *et al.* 1996). According to Foulger & Long (1984) and Foulger (1988), the pressure drop associated with the first event leads to a second event with opposite first-arrival polarity. These considerations motivate our interpretation of complex source spectra, with quasi-periodic notches at varying frequencies, as evidence for tensile opening and closing. In our case, the relatively short inferred time interval between opening and closing (a few milliseconds) precludes direct observation of distinct waveform arrivals, but nevertheless results in distinctive source spectral characteristics that may be indicative of complex rupture processes (Haddon & Adams 1997).

During a multistage hydraulic-fracture treatment, variations of fluid pressure with space and time are expected, involving variable stress state due to fracture development and fluid movement. Mixed modes of failure are expected when dealing with the heterogeneous stress field at the crack or fault tip, and/or heterogeneous media. For the 20 events analysed in detail here, we observed a range of  $S/P$  amplitude ratios including 17 events consistent with tensile failure ( $S/P < 5$ ). In addition, the events exhibiting complex source spectra are characterized by  $S/P$  amplitude ratios close to (or below) 2, indicating the occurrence of either pure tensile rupture or mixed mode (tensile + shear) failure (Walter & Brune 1993). This combination of source characteristics suggest that, for seismic frequencies, tensile events produced by hydraulic fracturing may include

a significant component of fractures opening and closing. The notching evident in Fig. 13 assumes superposition of two identical spectra with opposite sign. In reality, incomplete crack closure may reduce the amplitude of the second component in eq. (10), which would have the effect of diminishing the strength of the spectral notch. Likewise, a combination of (non-reversible?) shearing and tensile opening/closing (i.e. transtensional failure) may also affect the notch strength.

For the events characterized by complex rupture and low  $S/P$  values, Table 5 shows calculated source radius ( $a$ ) for tensile rupture computed solely based on moment magnitude using eq. (10). In this calculation, we have assumed an internal fluid pressure of 50 MPa, which is based on approximate fracture-propagation pressure derived from treatment curves provided for the hydraulic-fracture treatment. These estimates for source radius are generally consistent with fracture dimensions observed during mine-back experiments (e.g. Warpinski & Teufel 1991).

## CONCLUSIONS

Source magnitude and crack radius can be inferred by fitting far-field spectral models with observed spectra for microseismic events. We use models for shear events, together with a consistent model for tensile events derived by Walter & Brune (1993). Sensitivity analysis shows that reliable estimation of corner frequency for the observations distances in our study requires precise knowledge of

**Table 4.** Source parameters for microseismic events analysed using the Brune model, sorted by *S/P* amplitude ratio.

Event ID	<i>M<sub>w</sub></i>	<i>f<sub>c</sub></i> (Hz)	<i>S/P</i>	Distance (m)
A1-13	-1.06	Inf	8.9	358.8
A3-67	-1.48	225	6.0	299.2
A3-50	-0.95	248	5.0	477.9
A2-112	-1.22	Inf	4.7	360.9
A3-103	-1.19	1603	4.0	435.4
A3-56	-1.11	315	3.7	456.1
A3-98	-1.02	195	3.6	444.2
A2-61	-1.30	440	3.5	351.3
A2-135	-1.19	Inf	3.5	396.6
A2-74	-0.73	574	3.3	314.8
A2-184	-1.06	1084	3.0	478.4
A2-175	-1.71	344	2.7	311.6
A2-109	-1.19	765	2.3	398.1
A1-68	-1.70	363	2.2	299.2
<b>A4-21</b>	<b>-0.70</b>	<b>456</b>	<b>2.1</b>	<b>713.9</b>
<b>A3-106</b>	<b>-1.98</b>	<b>176</b>	<b>2.0</b>	<b>229.8</b>
<b>A7-6</b>	<b>-0.34</b>	<b>647</b>	<b>1.9</b>	<b>1512.4</b>
<b>A1-58</b>	<b>-1.82</b>	<b>207</b>	<b>1.8</b>	<b>292.6</b>
A1-151	-2.06	453	1.3	249.6
A6-2	-1.17	Inf	1.1	990.7

Note: Rows in bold have spectral characteristics consistent with composite (opening/closing) events.

**Table 5.** Source parameters for selected microseismic events with complex spectra, based on a tensile opening and closing model.

Event ID	<i>M<sub>w</sub></i>	<i>f<sub>c</sub></i> (Hz)	<i>S/P</i>	Distance (m)	$\tau$ (ms)	<i>a</i> <sup>1</sup> (m)
A4-21	-0.73	551	2.106	713.9	5.2	0.93
A3-106	-2.01	257	2.0048	229.8	5.5	0.21
A7-6	-0.51	1067	1.8979	1512.4	7.7	1.20
A1-58	-1.80	902	1.8244	292.6	6.0	0.27

Note: Source radius for tensile rupture based on eq. (1), assuming an internal fluid pressure of 50 MPa.

attenuation characteristics. Here, we apply our approach to microseismic data recorded during a hydraulic-fracture treatment in 2011 August in western Canada. Using one standard deviation in our measurements to represent uncertainty, we obtained  $Q_p = 109 \pm 46$  and  $Q_s = 101 \pm 46$ , based on recordings of perforation shots. Our  $Q$  sensitivity tests suggest that this level of uncertainty in  $Q$  precludes reliable determination of corner frequencies for microseismic source spectra. This limitation also precludes estimation of crack radius for shear events; however, for tensile events, where *a priori* knowledge of the internal pressure is available, the crack radius can be estimated without knowledge of the corner frequency. In particular, we have found the following relation relating crack radius to moment magnitude and internal pressure:  $\log_{10}(a) \approx 3.0 + 0.5M_w - \log_{10}(P_i)/3.0$ .

Low *S/P* spectral ratios have been proposed as a distinguishing characteristic of tensile events (Walter & Brune 1993). Analysis of 20 microseismic event spectra from our data set from western Canada shows that 17 have *S/P* spectral ratios  $<5$ , consistent with tensile rupture. Rapid opening/closing of a tensile fracture, or equal and opposite shear slip on a fault in rapid succession, will impart distinct spectral notches on the source spectrum that depend on the time interval  $\tau$  between opening and closing. Four of the events that we analysed contain spectral characteristics that are suggestive of this phenomenon.

## ACKNOWLEDGEMENTS

Sponsors of the Microseismic Industry Consortium are sincerely thanked for their support of this initiative. Arc Resources, Nanometrics and ESG Solutions are particularly thanked for its support of the Rolla Microseismic Experiment. Some of this work was completed while DWE was Benjamin Meaker Visiting Professor at the University of Bristol.

## REFERENCES

- Abercrombie, R.E., 1995. Earthquake source scaling relationships from  $-1$  to 5 ML using seismograms recorded at 2.5-km depth, *J. geophys. Res.*, **100**, 24 015–24 036.
- Aki, K. & Richards, P.G., 2002. *Quantitative Seismology*, 2nd edn, University Science Books.
- Atkinson, G., Kaka, S., Eaton, D., Bent, A., Peci, V. & Halchuk, S., 2008. A very close look at a moderate earthquake near Sudbury, Ontario, *Seismol. Res. Lett.*, **79**, 119–131.
- Baig, A. & Urbancic, T., 2010. Microseismic moment tensors: a path to understanding frac growth, *Leading Edge*, **29**, 320–324.
- Beresnev, I., 2001. What we can and cannot learn about earthquake sources from the spectra of seismic waves, *Bull. seism. Soc. Am.*, **91**, 397–400.
- Boore, D.M., 1983. Stochastic simulation of high-frequency ground motions based on seismological models of the radiated spectra, *Bull. seism. Soc. Am.*, **73**, 1865–1894.
- Boore, D.M. & Boatwright, J., 1984. Average body-wave radiation coefficients, *Bull. seism. Soc. Am.*, **74**, 1615–1621.
- Brune, J.N., 1970. Tectonic stress and the spectra of seismic shear waves from earthquakes, *J. geophys. Res.*, **75**, 4997–5009.
- Brune, J.N., 1971. Correction, *J. geophys. Res.*, **76**, 5002.
- Eaton, D.W. & Forouhdeh, F., 2011. Solid angles and the impact of receiver-array geometry on microseismic moment-tensor inversion, *Geophysics*, **76**, WC75–WC83.
- Eaton, D.W., van der Baan, M., Tary, J.-B., Birkelo, B., Spriggs, N., Cutten, S. & Pike, K., 2013. Broadband microseismic observations from a Montney hydraulic fracture treatment, northeastern B.C., Canada, *CSEG Recorder*, **38**, 44–54.
- Eshelby, J.D., 1957. The determination of the elastic field of an ellipsoidal inclusion and related problems, *Proc. R. Soc. Lond., A*, **241**, 376–396.
- Foulger, G.R., 1988. Hengill triple junction, SW Iceland: anomalous earthquake focal mechanisms and implications for process within the geothermal reservoir and at accretionary plate boundaries, *J. geophys. Res.*, **93**, 13 507–13 523.
- Foulger, G.R. & Long, R.E., 1984. Anomalous focal mechanisms: tensile crack formation on an accreting plate boundary, *Nature*, **310**, 43–45.
- Foulger, G.R., Julian, B.R., Hill, D.P., Pitt, A.M., Malin, P.E. & Shalev, E., 2004. Non-double-couple microearthquakes at Long Valley caldera, California, provide evidence for hydraulic fracturing, *J. Volc. Geotherm. Res.*, **132**, 45–71.
- Goertz-Allmann, B.P., Goertz, A. & Wiemer, S., 2010. Stress drop variations of induced earthquakes at the Basel geothermal site, *Geophys. Res. Lett.*, **38**, doi: 10.1029/2011GL047498.
- Haddon, R.A.W. & Adams, J., 1997. Anatomy of a small intraplate earthquake: a dissection of its rupture characteristics using regional data, *Geophys. J. Int.*, **129**, 235–251.
- Hanks, T.C. & Wyss, M., 1972. The use of body wave spectra in the determination of seismic source parameters, *Bull. seism. Soc. Am.*, **62**, 561–589.
- Hardebeck, J.L. & Shearer, P.M., 2003. Using *S/P* amplitude ratios to constrain the focal mechanisms of small earthquakes, *Bull. seism. Soc. Am.*, **93**, 2434–2444.
- Julian, B.R. & Foulger, G.R., 1996. Earthquake mechanisms from linear-programming inversion of seismic-wave amplitude ratios, *Bull. seism. Soc. Am.*, **86**, 972–980.
- Julian, B.R., Miller, A.D. & Foulger, G.R., 1996. Non-double-couple earthquakes. I. Theory, *Rev. Geophys.*, **36**, 525–549.
- Kisslinger, C., 1980. Evaluation of *S* to *P* amplitude ratios for determining focal mechanisms from regional network observations, *Bull. seism. Soc. Am.*, **70**, 999–1014.

- Kisslinger, C., Bowman, J.R. & Koch, L., 1981. Procedures for computing focal mechanisms from local (SV/P) data, *Bull. seism. Soc. Am.*, **71**, 1719–1729.
- Madariaga, R., 1976. Dynamics of an expanding circular fault, *Bull. seism. Soc. Am.*, **66**, 639–667.
- Madariaga, R., 1977. High frequency radiation from cracks (stress drop) models of earthquake faulting, *Geophys. J.*, **51**, 625–652.
- Majer, E.L. & Doe, T.W., 1986. Studying hydrofractures by high frequency seismic monitoring, *Int. J. Rock Mech. Min. Sci. Geomech. Abstr.*, **23**, 185–199.
- Miller, A.D., Julian, B.R. & Foulger, G.R., 1998. Three-dimensional seismic structure and moment tensors of non-double-couple earthquakes at the Hengill–Grensdalur volcanic complex, Iceland, *Geophys. J. Int.*, **133**, 309–325.
- Randall, M.J., 1973. The spectral theory of seismic sources, *Bull. seism. Soc. Am.*, **63**, 1133–1144.
- Sato, T. & Hirasawa, T., 1973. Body wave spectra from propagating shear cracks, *J. Phys. Earth*, **21**, 415–431.
- Shimizu, H., Sadato, U. & Koyama, J., 1987. A tensile-shear crack model for the mechanism of volcanic earthquakes, *Tectonophysics*, **144**, 287–300.
- Šilený, J., Hill, D.P., Eisner, L. & Cornet, F.H., 2009. Non-double-couple mechanisms of microearthquakes induced by hydraulic fracturing, *J. geophys. Res.*, **114**, B08307, doi:10.1029/2008JB005987.
- Sneddon, I.N., 1951. *Fourier Transforms*, McGraw-Hill.
- Song, F. & Toksöz, M.N., 2011. Full-waveform based complete moment tensor inversion and source parameter estimation from downhole microseismic data for hydrofracture monitoring, *Geophysics*, **76**, WC103–WC116.
- Stein, S. & Wysession, M., 2009. *An Introduction to Seismology, Earthquakes, and Earth Structure*, Blackwell Publishing.
- Tonn, R., 1991. The determination of the seismic Quality factor Q from VSP data: a comparison of different computational methods, *Geophys. Prospect.*, **39**, 1–27.
- Vavrycuk, V., 2001. Inversion for parameters of tensile earthquakes, *J. geophys. Res.*, **106**, 16 339–16 355.
- Walter, W.R. & Brune, J.N., 1993. Spectra of seismic radiation from a tensile crack, *J. geophys. Res.*, **98**, 4449–4459.
- Warpinski, N.R. & Du, J., 2010. Source-mechanism studies on microseismicity induced by hydraulic fracturing, in *SPE Annual Technical Conference and Exhibition*, Florence, Italy, Doc. ID 135254.
- Warpinski, N.R. & Teufel, L.W., 1991. In situ stress measurements at Rainer Mesa, Neva test site—influence of topography and lithology on stress state in Tuff, *Int. J. Rock Mech. Min. Sci. Geomech. Abstr.*, **28**, 143–161.

## APPENDIX A: SEISMIC MOMENT FOR SHEAR AND TENSILE FAILURE

In this appendix, we derive the relationship between the low-frequency plateau amplitude and seismic moment for both shear and tensile rupture. Consider a circular (penny shaped) crack of radius  $a$  lying in the  $x$ - $y$  plane (Fig. A1), subject to uniform shear stress  $\sigma_2$ . The relative displacement across the crack is given by (Eshelby 1957; Walter & Brune 1993)

$$\Delta u_2(r) = \frac{24\sigma_2}{7\pi\mu} \sqrt{a^2 - r^2} = \frac{\varepsilon_2}{a} \sqrt{a^2 - r^2}, \quad 0 \leq r \leq a, \quad (\text{A1})$$

where the displacement tapers to zero along the circumference of the crack ( $r = a$ ),  $\varepsilon_2$  is the maximum shear displacement across the crack at  $r = 0$ , and  $\mu$  is the shear modulus. In eq. (A1), it is also assumed that  $\lambda = \mu$ . The average shear displacement across the crack is  $2/3\varepsilon_2$  (Walter & Brune 1993).

Similarly, for a circular crack that fails under tension the net opening in the  $z$ -direction is given by (Sneddon 1951; Walter & Brune 1993)

$$\Delta u_3(r) = \frac{3P_1}{\pi\mu} \sqrt{a^2 - r^2} = \frac{\varepsilon_3}{a} \sqrt{a^2 - r^2}, \quad 0 \leq r \leq a, \quad (\text{A2})$$

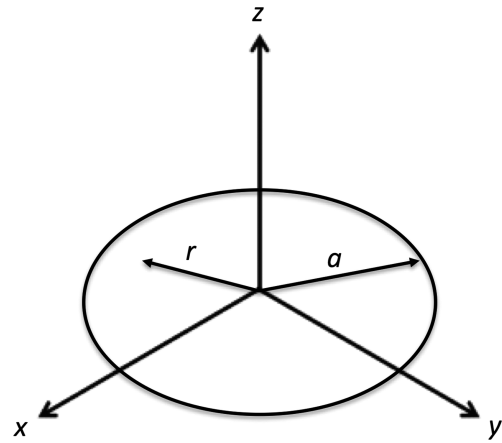


Figure A1. Geometry for a penny-shaped crack.

where  $P_1$  is the internal pressure within the crack (or equivalently, the tensile stress normal to the crack) and it is again assumed that  $\lambda = \mu$ . As in the previous case, the average displacement is  $2/3\varepsilon_3$ , where  $\varepsilon_3$  is the maximum opening at  $r = 0$ .

Seismic moment is given by (e.g. Aki & Richards 2002)

$$M_0 = \mu DS, \quad (\text{A3})$$

where  $D$  is the average displacement and  $S$  is the rupture area. From eq. (A1) and the average displacement  $2/3\varepsilon_2$ , in the case of shear rupture the seismic moment can be expressed in terms of the crack radius and shear stress as

$$M_0 = \mu \frac{16\sigma_2 a}{7\pi\mu} \pi a^2 = \frac{16}{7} \sigma_2 a^3. \quad (\text{A4})$$

From eq. (A2) and the average displacement  $2/3\varepsilon_3$ , in the case of tensile rupture the seismic moment can similarly be expressed in terms of the crack radius and internal pressure

$$M_0 = \mu \frac{2P_1 a}{\pi\mu} \pi a^2 = 2P_1 a^3. \quad (\text{A5})$$

Rearranging eqs (3) and (4), for the case of shear rupture we obtain

$$\sigma_2 a^3 = \frac{7\pi\rho c_v^3 |A_0^v| r}{4R_v}, \quad (\text{A6})$$

where  $R_v$  is the spherically averaged source radiation pattern,  $c_v$  is the applicable wave speed and  $A_0^v$  is the low-frequency plateau amplitude and  $v = P$  or  $S$  is the wave type. Combining eqs (A3) and (A4) yields the expression

$$M_0 = \frac{4\pi\rho c_v^3 |A_0^v| r}{R_v}, \quad (\text{A7})$$

which applies to shear rupture. Similarly, rearranging eqs (5) and (6), for the case of tensile failure we obtain

$$P_1 a^3 = \frac{2\pi\rho c_v^3 |A_0^v| r}{R_v}. \quad (\text{A8})$$

Combining (A5) with (A8) yields the same expression for seismic moment (A7) for the case of tensile failure. Finally, substituting (A5) into eq. (8) leads to the simple scaling relation

$$\log_{10}(a) = [9 - \log_{10} 2]/3 + 0.5M_w - \log_{10}(P_1)/3 \quad (\text{A9})$$

linking source radius to moment magnitude and internal fluid pressure.

## APPENDIX B: PROBABILITY DENSITY FOR $S/P$ AMPLITUDE RATIOS AND MAGNITUDE ESTIMATION ERRORS

In this appendix, we review the far-field radiation patterns for a general moment tensor,  $\mathbf{M}$  and discuss the probability distributions for amplitude ratio and magnitude. For a source located at the origin, the  $i$ th vector component of the  $P$ -wave amplitude, may be written (Eaton & Forouhdeh 2011)

$$u_i^P(\gamma) = (4\pi\rho\alpha^3)^{-1}[\gamma_i\gamma_j\gamma_k]M_{jk}, \quad (\text{B1})$$

where  $\rho$  and  $\alpha$  are density and  $P$ -wave velocity,  $\gamma$  specifies direction cosines of the propagation vector, and the summation convention for repeated indices is used. Similarly, the  $S$ -wave radiation pattern for a general moment tensor may be written as

$$u_i^S(\gamma) = (4\pi\rho\beta^3)^{-1}[(\delta_{ij} - \gamma_i\gamma_j)\gamma_k]M_{jk}, \quad (\text{B2})$$

where  $\beta$  is shear wave velocity and  $\delta_{ij}$  is the Kronecker delta. For a crack opening in the  $x_3$ -direction, the moment tensor for a pure tensile source (Julian *et al.* 1996)

$$M = \begin{bmatrix} \lambda & 0 & 0 \\ 0 & \lambda & 0 \\ 0 & 0 & \lambda + 2\mu \end{bmatrix}, \quad (\text{B3})$$

where  $\lambda$  and  $\mu$  are Lamé parameters. The tensile radiation pattern shown in Fig. 2 was computed using this expression with  $\lambda = \mu$ , whereas the shear radiation pattern in Fig. 2 was computed using

$$M = \begin{bmatrix} 0 & 1 & 0 \\ 1 & 0 & 0 \\ 0 & 0 & 0 \end{bmatrix}. \quad (\text{B4})$$

Probability density functions for  $S/P$  amplitude ratio (Fig. 3) were computed as follows. First,  $P$ - and  $S$ -wave radiation patterns were evaluated for uniform sampling of the focal sphere, with a sampling of  $4\pi/10^6$  sr. Excluding points on the focal sphere where either the  $P$ - or  $S$ -wave amplitude (or both) vanish, the amplitude ratio was computed using  $|\mathbf{u}^S|/|\mathbf{u}^P|$ . The complete set of amplitude ratio values was then binned in order to estimate the probability density, normalized to have an integrated value of unity.

Finally, based on eqs (7) and (8) the error in magnitude given by

$$E(\gamma) = \frac{2}{3} \log_{10} \left( \frac{\langle R_v(\gamma) \rangle}{\langle R_v \rangle} \right), \quad (\text{B5})$$

where  $\langle \rangle$  denotes average. The probability density for magnitude error is then estimated in the same way as the  $S/P$  amplitude ratio.

## SUPPORTING INFORMATION

Additional Supporting Information may be found in the online version of this article:

**Table S1.** Details of Qp calculations.

**Table S2.** Details of Qs calculations.

(<http://gji.oxfordjournals.org/lookup/suppl/doi:10.1093/gji/ggt498/-/DC1>).

Please note: Oxford University Press are not responsible for the content or functionality of any supporting materials supplied by the authors. Any queries (other than missing material) should be directed to the corresponding author for the article.